Cell Reports
Supplemental Information

α-tubulin tyrosination and CLIP-170 phosphorylation regulate the initiation of dynein-driven transport in neurons

Jeffrey J. Nirschl, Maria M. Magiera, Jacob E. Lazarus, Carsten Janke, Erika L. F. Holzbaur

Supplemental Figure Legends

Figure S1, related to Figure 1

Supplementary data for Figure 1. (A) Deconvolved max projection confocal images of COS-7 cells transfected with HaloTag (HT) CLIP-170 (WT, A, E) and stained for the HT epitope. Phosphodeficient CLIP-A comets are significantly longer than phosphomimetic CLIP-E as shown previously (Lee et al. 2010); this comparison shows the dynamic range of CLIP-170 phosphorylation. (B) Bootstrapped mean and 95% confidence intervals (CI) for line scans of CLIP-170 comets (n > 60 comets per condition from 4 cells, N = 2). (C) Mean $p150^{Glued}$ intensity per cell for $p150^{Glued}$ WT or G71R shows similar levels of recombinant protein expression (n > 40 cells, N=2). (D) Representative dSTORM image of HT-CLIP-A comets decorated with myc-$p150^{Glued}$ WT.

Figure S1

A

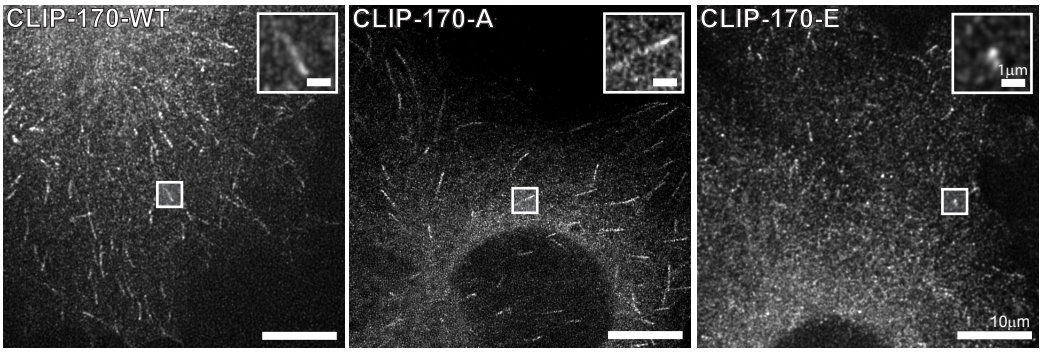

B

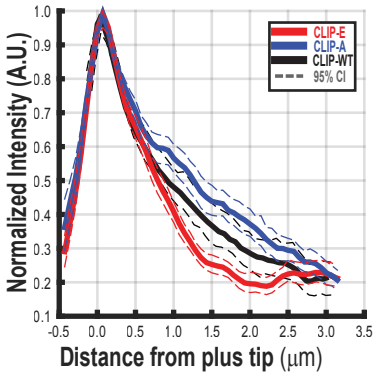

C

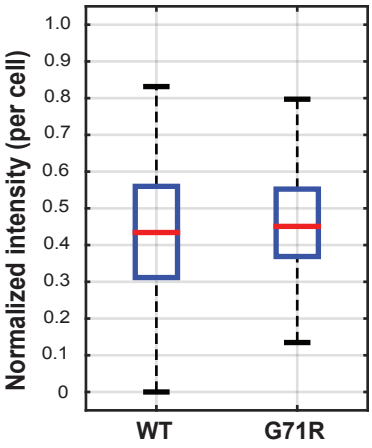

D

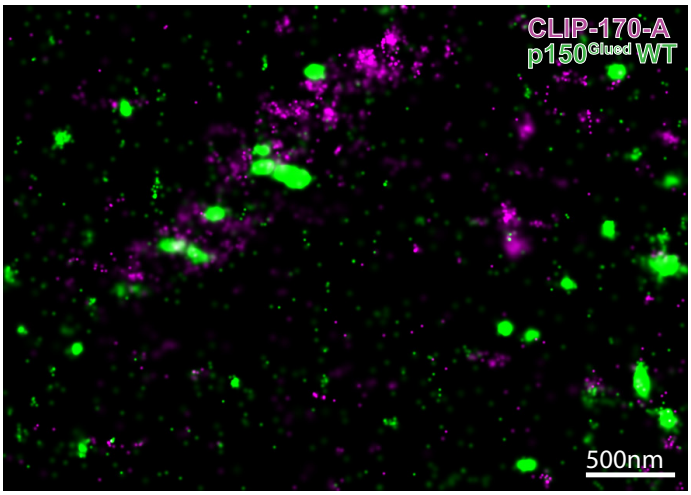

Figure S2, related to Figures 2 and 5

Western blot characterization of neuronal vesicles, related to Figures 2 and 5. Western blot of isolated neuronal vesicles shows a robust population of vesicles similar to Hendricks et al. 2010. Fractions were blotted for antibodies to dynein heavy chain (DHC), dynein intermediate chain (DIC), $p150^{Glued}$, p50-GFP, Lis1, kinesin-1 heavy chain (KHC), kinesin-2, LAMP-1, synaptotagmin, beta-tubulin, and GAPDH. Cytosolic marker GAPDH is not enriched in the vesicle fraction.

Figure S2

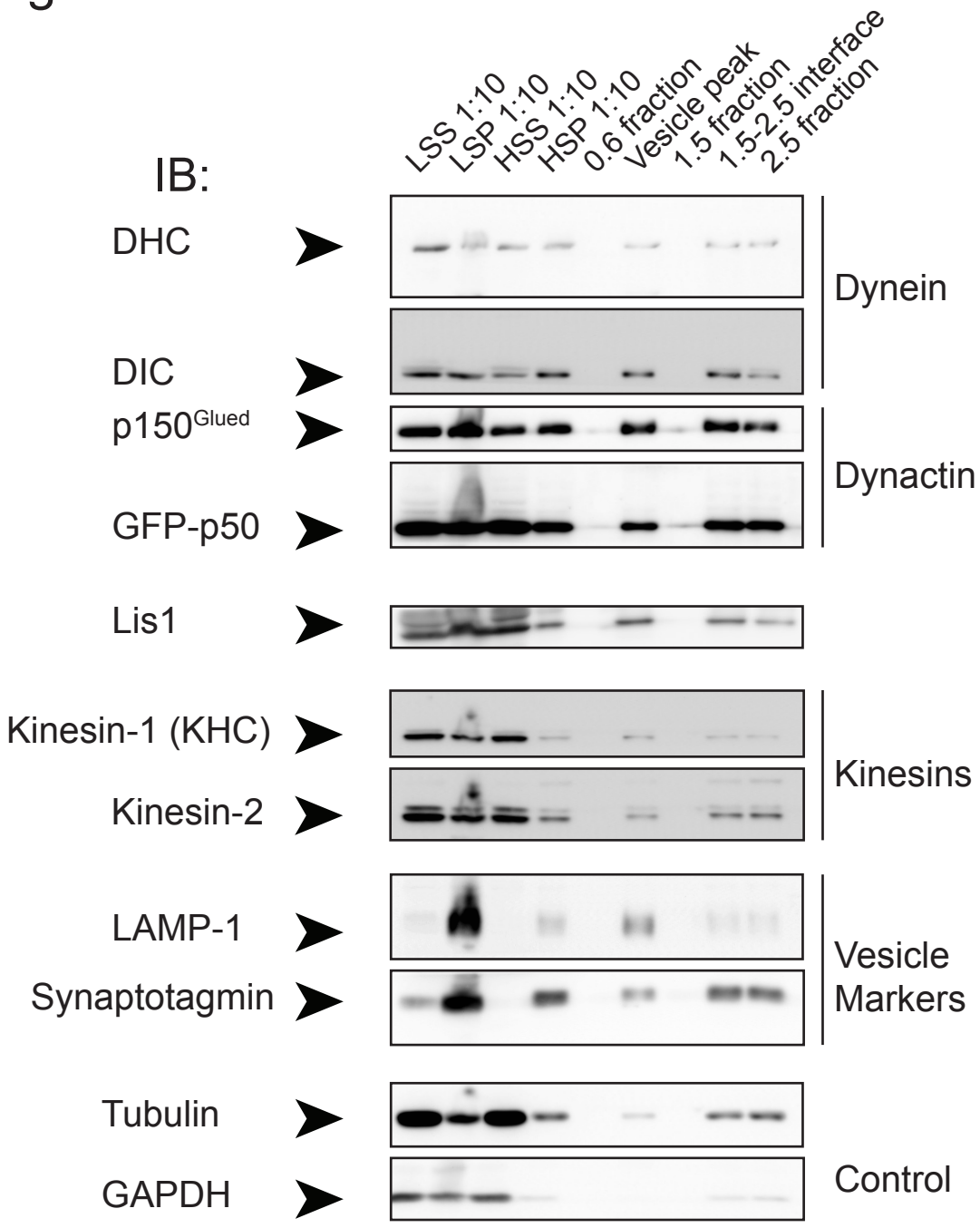
LSS 1:10
LSP 1:10
HSS 1:10
HSP 1:10
0.6 fraction
Vesicle peak
1.5 fraction
1.5-2.5 interface
2.5 fraction
IB:
DHC
DIC
p150Glued
GFP-p50
Lis1
Kinesin-1 (KHC)
Kinesin-2
LAMP-1
Synaptotagmin
Tubulin
GAPDH
Dynein
Dynactin
Kinesins
Vesicle Markers
Control

Figure S3, related to Figure 2

Supplementary data for Figure 2. (A) Standard curve of the absorbance (555nm) of tetramethylrhodamine (TMR) in lysis buffer (mean + SD; n = 10, N = 3). (B) Spectrum sweep showing the absorbance of TMR standard in lysis buffer vs mock-transfected cell lysates at different wavelengths. At 555nm, cytosolic proteins in cell lysates have very low absorbance and thus minimally interfere with TMR measurements used in the assay to determine relative concentration of TMR-labeled proteins in cell lysates. (C) Western blot of cell extract HSS for TMR labeled CLIP-WT, CLIP-A, and CLIP-E. Densitometry analysis, normalized to WT condition, shows similar levels of HT-CLIP protein in cell lysates (mean +SD). (D) Western blot of cell extract HSS shows similar levels of expression of EB1, Lis1, and $p150^{Glued}$ regardless of the recombinant CLIP-170 construct. (E) Above, the still images from TIRF movies with 100nM unlabeled EB1 + ~100nM CLIP in the lysate HSS. CLIP-E shows very little microtubule decoration whereas CLIP-A robustly decorates GMPCPP microtubules. Below, the still images from TIRF show 100nM Rhodamine labeled EB1 decorating GMPCPP microtubules. (F) Schematic of computational image analysis workflow. Additional details provided in the Supplemental Experimental Procedures. (G) Parameter sweep of uTrack thresholds for local maxima detection show a stable number of particles is detected with a local maxima threshold of 0.01 for a single frame or 0.005 for over a window of 3 frames (green line). At this threshold, the median SNR for detected particles is 4.1, which is within acceptable limits for many single-particle tracking algorithms (Chenouard et al. 2014).

Figure S3

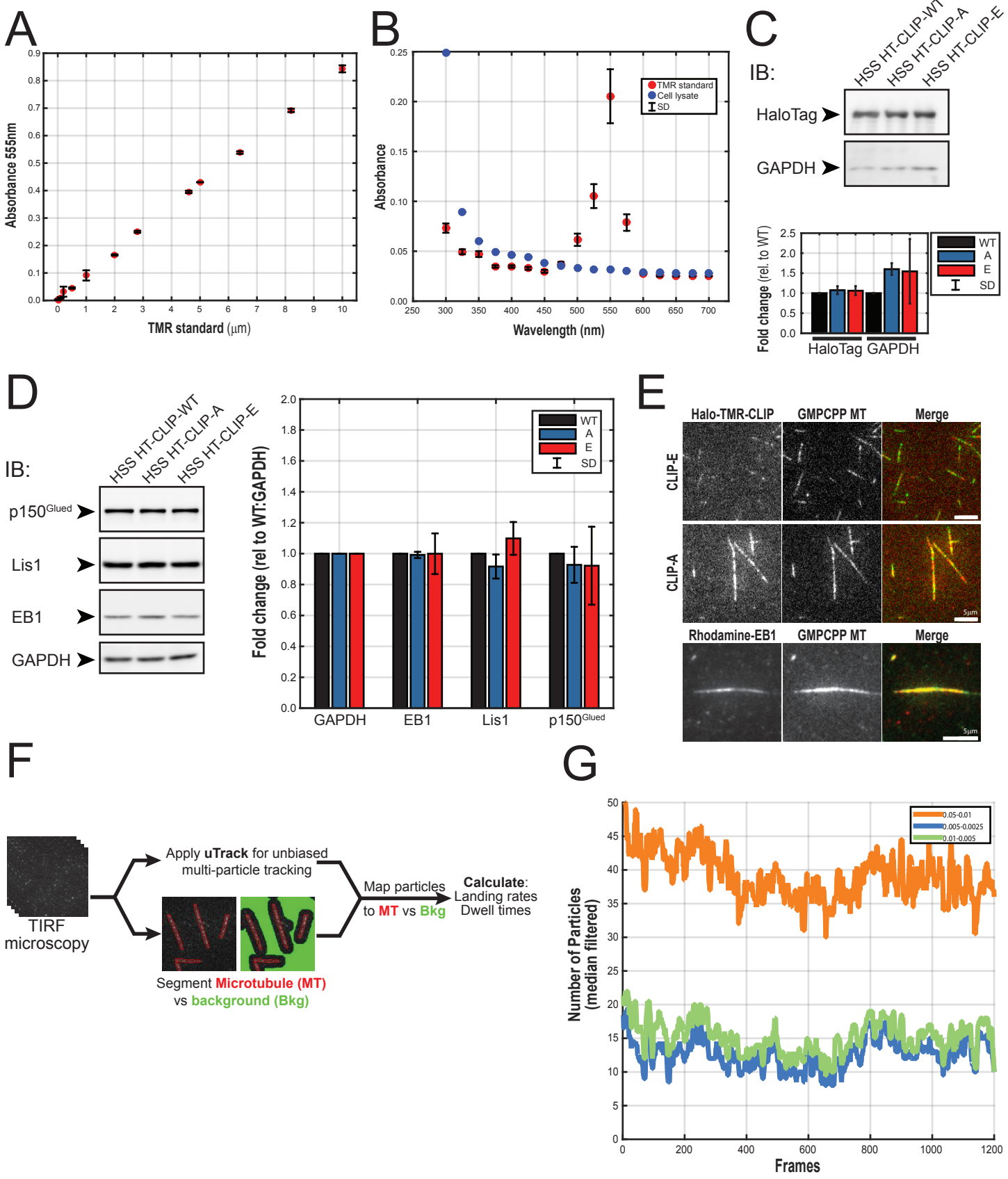
A
Absorbance 555nm
TMR standard (μm)
B
Absorbance
Wavelength (nm)
TMR standard
Cell lysate
SD
C
IB:
HSS HT-CLIP-WT
HSS HT-CLIP-A
HSS HT-CLIP-E
HaloTag
GAPDH
Fold change (rel. to WT)
WT
A
E
SD
HaloTag
GAPDH
D
IB:
HSS HT-CLIP-WT
HSS HT-CLIP-A
HSS HT-CLIP-E
p150Glued
Lis1
EB1
GAPDH
Fold change (rel to WT:GAPDH)
WT
A
E
SD
GAPDH
EB1
Lis1
p150Glued
E
Halo-TMR-CLIP
GMPCPP MT
Merge
CLIP-E
CLIP-A
5μm
Rhodamine-EB1
GMPCPP MT
Merge
5μm
F
TIRF microscopy
Apply uTrack for unbiased multi-particle tracking
Segment Microtubule (MT) vs background (Bkg)
Map particles to MT vs Bkg
Calculate: Landing rates Dwell times
G
Number of Particles (median filtered)
Frames
0.05-0.01
0.005-0.0025
0.01-0.005

Figure S4, related to Figure 3
Supplementary data for Figure 3. Quantification of the median normalized intensity per neuron for the Oregon Green-labeled CLIP rescue constructs. These data are from the same neurons used for measuring retrograde flux in Figure 3B, C and demonstrate that all rescue constructs expressed to similar levels. Intensity was normalized to the min/max of the entire dataset of all conditions.

Figure S4

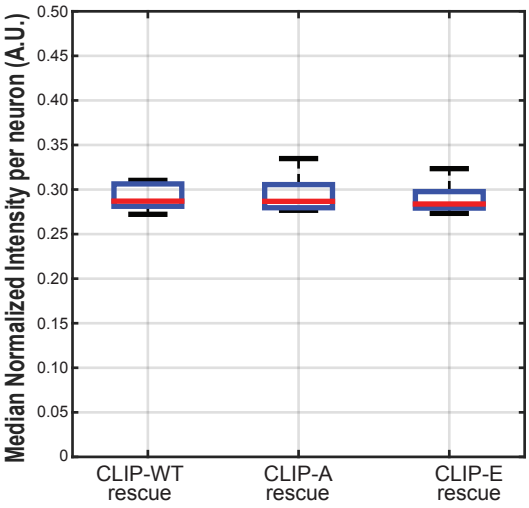
Median Normalized Intensity per neuron (A.U.)
0.50
0.45
0.40
0.35
0.30
0.25
0.20
0.15
0.10
0.05
0
CLIP-WT rescue
CLIP-A rescue
CLIP-E rescue

Figure S5, related to Figure 5

Supplementary data for Figure 5. (A) Histogram of the microtubule lengths for GMPCPP microtubules polymerized with purified Tyr-/Detyr-tubulin. Each dataset was normalized to its Probability Density Function (PDF); distributions were compared with a two-sample KS test ($p = 0.11$; $n > 1400$ microtubules per condition total; $N = 3$). (B) Quantification of landing rate for Tyr-/ Detyr microtubules, separated by the fluorescently labeled tubulin used, shows a significant increase in landing rate on Tyr microtubules regardless of labeled tubulin ($n > 30$ movies per condition, each movie with > 500 events; $N = 3$ independent vesicle isolations; Kruskal-Wallis one way ANOVA with Tukey-Kramer post-tests). (C) Histogram of the normalized PDF of dwell times on TRITC or AF647 labeled Detyr-microtubules show overlap of the distributions. (D) Histogram of the normalized PDF of dwell times on TRITC or AF647 labeled Tyr-microtubules show overlap of the distributions.

Figure S5

A

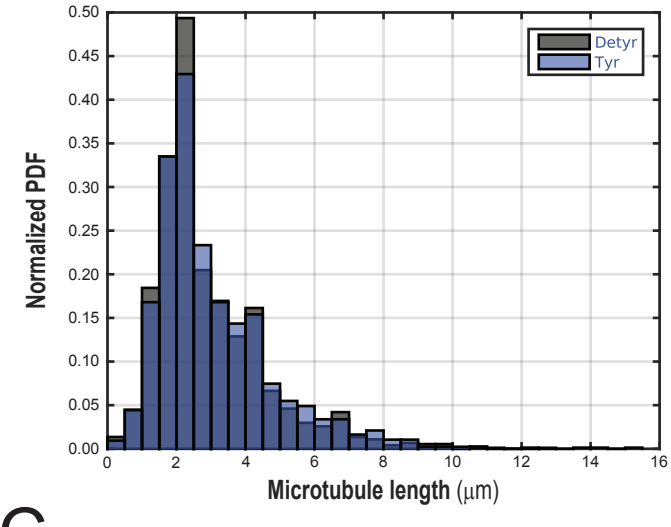

B

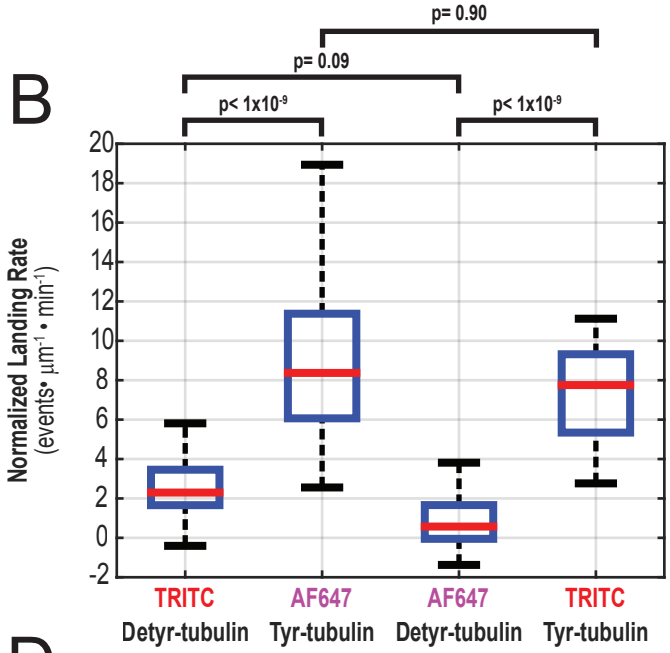

C

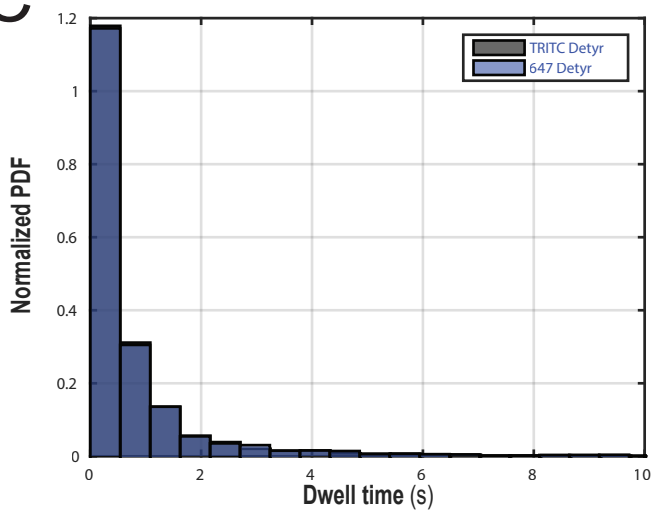

D

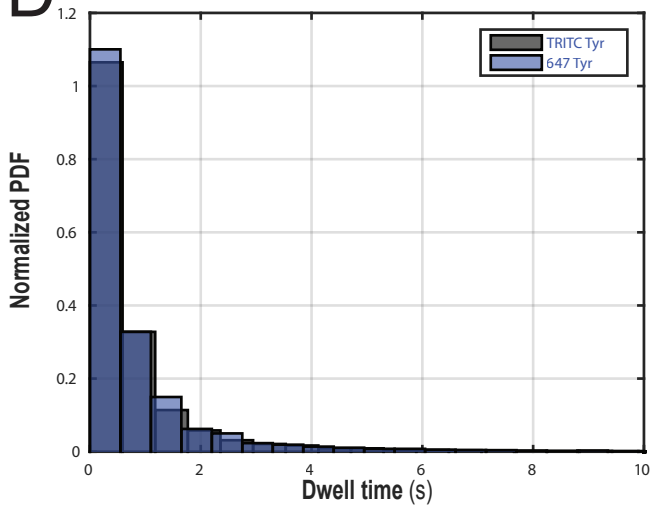

Figure S6, related to Figure 6

Supplementary data for Figure 6. Coomassie stained gel of purified proteins, including EB1, CLIP-170-H2-GFP, p150$^{Glued\ [1-210]}$-GFP, p150^{Glued} ΔBasic $^{[1-210]}$-GFP, p150^{Glued} ΔCAP-Gly $^{[1-210]}$-GFP, and CA-Kinesin-1$^{[1-430]}$-GFP.

Figure S6

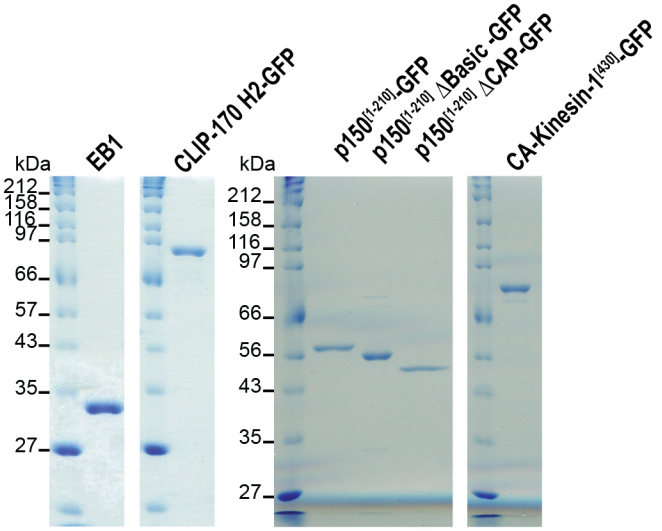
kDa
EB1
CLIP-170 H2-GFP
kDa
p150[1-210]-GFP
p150[1-210] ΔBasic -GFP
p150[1-210] ΔCAP-GFP
CA-Kinesin-1[430]-GFP
212
158
116
97
66
57
43
35
27
212
158
116
97
66
56
43
35
27

Figure S7, related to Figure 7

Supplementary data for Figure 7. (A) Pseudocode for Monte Carlo simulation of 2D vesicle diffusion and microtubule capture. Parameters: timeStep = 0.1s, D = 0.006μm^2/s, D_Std= sqrt(2*D*timeStep), Prob(Tyr) = 1, Prob(Detyr) = 0.25, MaxDuration = 1200 s. PM refers to the plasma membrane. (B) Quantification of the median time to MT capture with Tyr probabilities and CLIP-E or CLIP-A at diffusion coefficients 0.05 – 1.0μm^2/s. (C) Scatter plot of the time to MT capture given the initial starting distance from the microtubule with Tyr probabilities and CLIP-E or CLIP-A at a diffusion constant 0.006μm^2/s. There was a 2.4 fold increase in the number of CLIP-E (red arrowhead) particles that never reach the microtubule within a 20 minute simulation with as compared to CLIP-A (blue arrowhead). (D) The bootstrapped mean and 95% confidence intervals for the time to MT at each starting distance are plotted below. The two lines overlap and the time to capture in these simulations is determined by the initial distance. Thus, the effect of CLIP-A is due to a shift in the distribution of starting positions such that they are, on average, closer to the effective microtubule capture zone.

Figure S7

A

Stochastic simulation of 2D diffusion and MT capture

```
1)  Set parameters (D, D_Std N, Prob, MaxDuration)
2)  FOR  trajectory 1: N
3)      Randomly assign starting index in growth cone
4)          FOR  iteration 1 : MaxDuration
5)              Check location (Cytosol, MT, PM)
6)              IF  Cytosol
7)                  Generate next step from a
                    normal distribution (μ=D, σ=D_Std)
8)              ELSEIF  MT
                    CheckBind = unif. rand. var [0,1]
                    IF CheckBind <= Prob
                        End simulation for track
                    ELSE
                        Generate next step
                        (μ=D, σ=D_Std)
                    END
9)              ELSEIF  PM
                    Pause at PM for current step, then
                    move away from PM next step
                END
10)         END
11) END
```

B

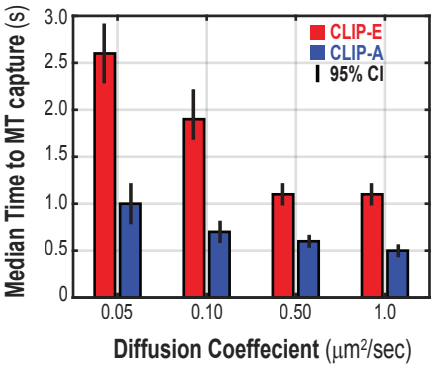

C

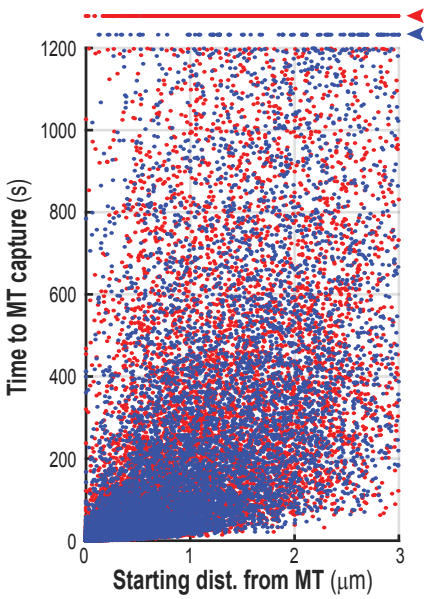

D

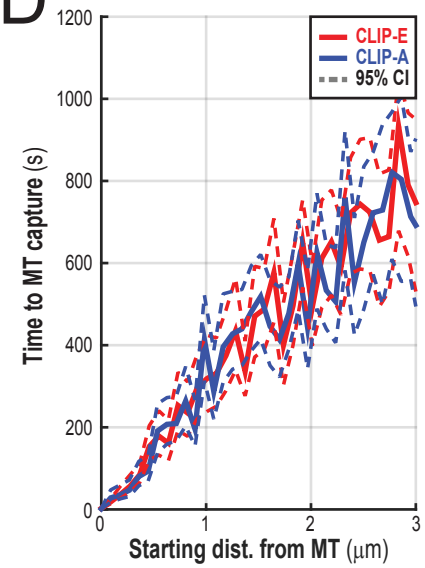

Supplemental Tables

Table S1, related to Figure 3

Kruskal-Wallis one-way ANOVA and Tukey-Kramer post-hoc tests between groups for data in Figure 3C.

Kruskal-Wallis one-way analysis of variance

Chi-sq: 29.4

df: 4

p: 6.50×10^{-6}

Tukey-Kramer post-hoc test between groups

Groups being compared:		p value
1	2	0.002107
1	3	0.999890
1	4	0.997870
1	5	0.216500
2	3	0.000094
2	4	0.000204
2	5	0.271370
3	4	0.999570
3	5	0.100470
4	5	0.155260

Number	Condition
1	Mock siRNA
2	siRNA + Vector
3	siRNA + CLIP-WT
4	siRNA + CLIP-A
5	siRNA + CLIP-E

Table S2, related to Figure 6

Kruskal-Wallis one-way ANOVA and Tukey-Kramer post-hoc tests between groups for data in Figure 6B.

Kruskal-Wallis one-way analysis of variance

Chi-sq: 137.87

df: 7

p: 1.42×10^{-26}

Tukey-Kramer post-hoc test between groups

Groups being compared:		p value
1	2	6.0033×10^{-8}
1	3	0.99998
1	4	5.9893×10^{-8}
1	5	0.99996
1	6	0.08692
1	7	0.00001
1	8	0.00034
2	3	6.0433×10^{-8}
2	4	1.00000
2	5	5.9882×10^{-8}
2	6	0.00040
2	7	0.56326
2	8	0.16285
3	4	5.9927×10^{-8}
3	5	0.99633
3	6	0.17335
3	7	0.00003
3	8	0.00095
4	5	5.9881×10^{-8}
4	6	0.00010
4	7	0.40957
4	8	0.08941
5	6	0.01853
5	7	4.8394×10^{-7}
5	8	0.00002
6	7	0.23258
6	8	0.69481
7	8	0.99683

Number	Protein	Tyr/ Detyr
1	CLIP-WT	Detyr
2	CLIP-WT	Tyr
3	CLIP-A	Detyr
4	CLIP-A	Tyr
5	CLIP-E	Detyr
6	CLIP-E	Tyr
7	CA-Kinesin-1$^{[560]}$	Detyr
8	CA-Kinesin-1$^{[560]}$	Tyr

Supplemental Movies

Movie S1, related to Figure 1

STORM 3D reconstruction of WT p150^{Glued} puncta associated with a CLIP-A comet at the microtubule plus end, related to Figure 1. This represents a cropped view of a single microtubule plus end (unlabeled) in COS-7 cells expressing myc-p150^{Glued} WT and HT-CLIP-A. CLIP-A decorates the microtubule plus end as long comets, which is shown in magenta. Wild type p150^{Glued} forms either discrete clusters of p150^{Glued} that dock on the CLIP-A comet and correspond to the p150^{Glued}-positive puncta identified by confocal microscopy. In addition, a soluble pool of point-localized p150^{Glued} also localize to the CLIP-A comet.

Movie S2, related to Figure 5

Robust p50-GFP-vesicle recruitment to Tyr microtubules. Alexa647-labeled Tyr microtubules are shown in magenta, related to Figure 5. TRITC-labeled Detyr microtubules are shown in red. The Green-Fire-Blue lookup table was applied to GFP-vesicles for better visualization. Playback is 2x real time (20fps).

Movie S3, related to Figures 5 and S5

p50-GFP-vesicle recruitment to Tyr microtubules is independent of the fluorescent tubulin label, related to Figures 5 and S5. TRITC-labeled Tyr microtubules are shown in red. Alexa647-labeled Detyr microtubules are shown in blue. The Green-Fire-Blue lookup table was applied to p50-GFP-vesicles for better visualization. Playback is 2x real time (20fps).

Movie S4, related to Figure 6

Representative movies for CLIP-WT/ -A/ -E recruitment to Tyr or Detyr-microtubules. TMR-HaloTag-CLIP-170 is shown in red; Alexa488 Tyr-microtubules in green; and Alexa647 Detyr-microtubules in blue. The Alexa labeled tubulin used for Tyr/ Detyr-microtubules was reversed for half of the experimental repeats with similar results. Playback is 2x real time (20fps).

Supplemental Experimental Procedures

Microscopy

Single-molecule imaging was performed on an inverted Nikon Ti Eclipse equipped for total internal fluorescence (TIRF) microscope with a cooled Hamamatsu ImagEM charge-coupled device (CCD) camera C9100-13 using a 1.45 N.A. x100 oil immersion objective with an effective pixel size of 159nm. Single molecule imaging acquired the channel of interest at a rate of 10 frames per second for 2 minutes, with still images of microtubule captured at 0 and 2 minutes. Exposure times were 75ms and laser intensities were kept constant whenever conditions were compared. Spinning disk confocal microscopy was performed on an inverted Nikon Ti Eclipse with a Perkin-Elmer Ultra VIEW Vox spinning disk confocal module and a PhotoKinesis accessory for photobleaching. Images were acquired with a Hamamatsu ImagEM CCD camera E9100-50 using a 1.45 N.A. x100 oil immersion objective with an effective pixel size of 71.5nm. STED microscopy was performed on a Leica DMI 6000 inverted microscope equipped with 592nm and 660nm STED depletion lasers. Direct STORM was performed on a Nikon STORM system.

Reagents

Antibodies: CLIP-170, rabbit polyclonal (CST #8977); anti-HaloTag, rabbit polyclonal (Promega #G9281); anti-GAPDH, mouse monoclonal (Abcam ab9484); anti-Tyr-alpha-tubulin YL1/2, rat monoclonal (Milipore #1864); anti-Detyr-alpha-tubulin, rabbit polyclonal (Milipore #AB3201); anti-beta-tubulin mouse monoclonal clone TUB2.1 (Sigma T5201); anti-synaptotagmin, mouse monoclonal (StressGen SYA-130); anti-Rab7, mouse monoclonal (Abcam ab50533); anti-LAMP-1, rabbit polyclonal (Abcam ab24170); GFP-Booster (Chromotek gba488); anti-p150^{Glued} CAP-Gly, mouse monoclonal (BD Transduction 610474); anti-dynein heavy chain, rabbit polyclonal (sc-9115); anti-DIC (Milipore #1618); anti-KIF5B, mouse monoclonal (Milipore #1614); anti-KIF3A (Abcam ab24626); anti-GFP, chicken (Clontech JL-8); anti-Lis1, mouse (Sigma #L7391); anti-EB1, mouse (BD Transduction 610534).

siRNA: Mouse CLIP1 siRNA (Dharmacon: J-054772-10, CUUCAAAGCUAACGAGGAA; and J-054772-11 GCAGAAGAGUAUUGGCGAA). Control non-targeting siRNA pool (Dharmacon: D001810-01-05).

DNA Constructs: LAMP-1-RFP (Addgene #1817). Rat CLIP-170 (AJ237670.1) was used to generate a wild-type CLIP-1 construct fused to HaloTag® at the N terminus. Serine residues (309, 311, 313, 319, 320) of this CLIP-170 construct were mutated to glutamate (phosphomimetic, CLIP-E) or alanine (phosphodeficient, CLIP-A). Human p150^{Glued} (NM_004082.4) fused to an N-terminal myc tag. Human KIF5C amino acids 1-560 fused to an N-terminal HaloTag®, derived from Addgene #15219.

Cell culture and live-cell imaging

DRG neurons were transfected with LAMP-1-RFP (0.3ug), siRNA resistant rat HT-CLIP-170 or HT-vector (0.5ug), Mouse CLIP-1 siRNA (20pmol) and then cultured for 4DIV. The distal axon of DRG neurons were imaged in a temperature-controlled chamber at 37C. After identifying the distal axon, a 40μm region of axon that is 10μm proximal to the growth cone tip was photobleached a 561nm laser at 100%, allowing measurement of retrograde flux through a pre-defined region 3.5μm proximal to the distal edge of the bleached region. Movies were acquired at 200ms per frame for 2fps for 5s pre-bleach and 2fps for 120s post-bleach.

Protein biochemistry

Unlabeled tubulin was purified from bovine brain through two cycles of polymerization and depolymerization in high-molarity PIPES buffer as described (Castoldi & Popov 2003). EB1, CLIP-170-H2, and GFP-p150^{Glued} constructs were purified as described (Lazarus et al., 2013). Protein concentrations were determined using BCA or A280nm (tubulin).

Tyrosinated tubulin was obtained from Hela S3 cells (ATCC® CCL-2.2™) according to the protocol adapted from (Barisic et al., 2015; Castoldi & Popov, 2003). Cells were grown in the spinner bottles for 1 week, then spun down and lysed in BRB80 (80 mM K-PIPES pH 6.8, 1 mM MgCl2, 1 mM EGTA) supplemented with 1 mM β-mercapthoethanol, 1 mM PMSF and protease inhibitors using a French Press at 4°C. The soluble fraction was obtained after ultracentrifugation and the first tubulin polymerization step was performed at 30°C for 30 min by adding 1 mM GTP and 30% glycerol. Microtubules were pelleted by ultracentrifugation at 30°C, and then re-suspended in BRB80 at 4°C; soluble tubulin was clarified by ultracentrifugation at 4°C. Carboxypeptidase A (CPA, Sigma C9268, app 6U/mg of tubulin) was added to the soluble tubulin for 5 min at 30°C to produce detyrosinated tubulin. The second polymerization, this time in presence of high molarity PIPES, was performed for 30 min at 30°C and the microtubule pellet was sedimented by ultracentrifugation. Microtubules were then depolymerized in BRB80 at 4°C, and soluble tubulin clarified and snap frozen. The tyrosination status of the tubulin was verified by Western blot using the antibodies against tyrosinated (YL1/2) and detyrosinated (Millipore, AB3201) tubulin.

In vitro reconstitution of microtubule recruitment

Briefly, adult mouse brains were homogenized in ice-cold MAB with 1mM dithiothreitol (DTT) and protease inhibitors. The homogenate was centrifuged first at 17K x g for 30 minutes, and then at 133K x g for 20min to pellet the lower density membrane fraction. The membrane pellet was loaded onto the bottom of a sucrose step gradient (2.5M, 1.5M, 0.6M) and centrifuged at 274K x g, and vesicles were collected from the 1.5M - 0.6M interface.

Image analysis and machine learning classification of fixed particles

Our unbiased multi-particle tracking approach provides a robust, automated method to determine landing rates while correcting for the background rate of particles randomly entering the TIRF field. Particle tracking was performed in uTrack (v.2.1.3). The median particle SNR was 4.1, which is within acceptable limits for most single-particle tracking algorithms (Chenouard et al., 2014). Microtubule (MT) masks were generated by applying a pixel classifier in ilastik (Sommer et al., 2011) to create a probability map, which was further processed using custom MATLAB scripts to segment individual MT from the background. Unambiguous labeling of events in the MT or background was ensured by creating a buffer region of 10 pixels surrounding each MT; particles landing in this region were excluded from analysis. Overlapping MTs were excluded from analysis. Particle trajectories were mapped onto their positions within MT or background masks to determine the landing rate, per square micron per minute. This gave one MT landing rate and one background landing rate per movie and allowed the subtraction of the background landing rate to obtain the normalized landing rate per square micron. Since the microtubule has a fixed intensity profile width of ~3 pixels in our images, we used a conversion factor to transform the landing rate per square micron to the landing rate per micron length. Calculating the whole-field landing rate per movie gave more precise values than calculating a per microtubule landing rate, which were subject to extreme values. However, neither method of calculating landing rate significantly changed the results. To minimize the contribution of random landing events on our measurements we used a low density of microtubules in our flow chambers. On average, less than 10% of the image field contained microtubules. Assuming that non-specific landing events have a uniform random probability of landing at any given pixel, this reduced the number of non-specific events relative to the total number of events observed.

There was a class of particles landing in the background with long dwell times and little displacement, which we label as particles fixed to the coverslip. These particles had the potential to skew our dwell time analysis, and to correct for this we used a machine learning approach to detect and exclude these fixed particles from analysis. In brief, we used a Random Forest classifier in MATLAB consisting of 2000 trees and trained on 898 trajectories manually labeled as fixed to the coverslip (0) or not-fixed (1) with 22 features derived from the XY coordinates and intensity for each trajectory. The generalization error from held-out examples in the training set was ~ 5% and the classifier had a 95.5% AUC on a held-out test set of 100 examples.

Stochastic simulation of 2D organelle diffusion and microtubule capture

Immunofluorescence images of tyrosinated microtubules and a cytosol-filling marker were used to create the experimental space for simulated trajectories. Briefly, an ilastik pixel-level classifier on the MT intensity image was used to segment microtubules in the growth cone, which was manually refined for a best-fit segmentation. Similarly, ilastik was used on the combined MT and GFP-LC3 intensity image to segment the neuron outline. These two masks formed the experimental space for simulated vesicle diffusion and microtubule capture. For each neuronal growth cone, 1000 trajectories were

generated and seeded at random starting indices. Each trajectory underwent simulated 2D Brownian diffusion with a time interval of 0.1s for 1200 seconds simulated time. At each time step, the current position of the trajectory in simulation space was evaluated accordingly: cytosol = continue simulation; MT = end simulation for current trajectory; plasma membrane = pause for 0.1s and then move away from PM in the next step. To simulate the diffusion of a large organelle in the heterogeneous viscoelastic environment of the cytoplasm, we used a diffusion constant, D = 0.006 μm2/s, taken from empirical measurements of the diffusion of EGF-quantum-dot labeled endosomes in the Arpe-19 cell cytoplasm (Zajac, Goldman, Holzbaur, & Ostap, 2013). This value is similar to the diffusion of non-microtubule bound melanosomes (D = 0.003 μm^2/sec) in Xenopus melanophores (Semenova et al., 2008). We also simulated a range of diffusion constants from 0.001 to 1.0μm^2/s (Figure S7).

To simulate retrograde flux for comparison with our experimental observations, we first measured the number of LAMP-1-RFP vesicles within of the 10μm distal axon growth cone of WT DRG neurons expressing LAMP-1-RFP at low levels. The empirical distribution of LAMP-1-RFP vesicles had a mean of 12 and SD of 6 and approximated a normal distribution (n = 30 neurons; $p > 0.1$, one-sample KS test). We randomly sampled this distribution to determine the random number of vesicles (nVesicles) we may expect to find in any given growth cone. Next we sampled nVesicles, with replacement, from a pool of 5,000 simulated vesicles per neuron and calculated the number of vesicles that reach the microtubule within the duration of our neuronal live cell imaging experiment (120 sec). Since we measure retrograde flux 3.5μm proximal to the bleached region, a vesicle only counted toward retrograde flux if it reached the microtubule within 120 sec – (3.5μm / 0.5μm/sec), or 113 sec, which assumes cargo undergoes continuous, processive dynein driven transport at a velocity of 0.5μm/sec following microtubule capture. As biological cargo may not capture with 100% efficiency or may exhibit directional changes, these simulations may slightly overestimate retrograde flux. The simulation for each neuron growth cone was repeated 5000 times per condition.

Statistics

Statistical tests and distribution fitting were performed in MATLAB R2015a. A Wilcoxon Rank-Sum test was used to compare two sample medians and the Kruskal-Wallis one-way ANOVA was used to compare multiple medians, with a Tukey-Kramer post-test used to correct for multiple comparisons between sample medians. A two sample Kolmogorov-Smirnov test was used to compare two distributions, with Bonferroni correction for pairwise comparison of multiple distributions. The 95% confidence intervals (CI) were calculated from 1000 bootstrapped resamplings. Maximum likelihood estimation with 100 bootstrapped fits was used to fit dwell times with a double exponential curve and obtain 95% CI on the curve parameters (amplitude, k1, and k2). Box and whisker plots show the median (red bar) and interquartile range (IQR, blue box) with the whiskers extending to the upper and lower adjacent values. Statistical outliers, defined as data greater than median +/- 1.5*IQR, were included in all analysis, but are not shown in boxplots so that the outliers do not compress the visualization of the majority of data.

Supplemental References

Barisic, M., Silva, R., Tripathy, S. K., Magiera, M. M., Zaytsev, A. V, Pereira, A. L., … Maiato, H. (2015). Microtubule detyrosination guides chromosomes during mitosis. *Science*, *1*(April), 1–9. http://doi.org/10.1017/CBO9781107415324.004

Castoldi, M., & Popov, A. V. (2003). Purification of brain tubulin through two cycles of polymerization-depolymerization in a high-molarity buffer. *Protein Expression and Purification*, *32*(1), 83–8. http://doi.org/10.1016/S1046-5928(03)00218-3

Chenouard, N., Smal, I., de Chaumont, F., Maška, M., Sbalzarini, I. F., Gong, Y., … de Solórzano, C. O. (2014). Objective comparison of particle tracking methods. *Nature Methods*, *11*(3), 281–290. http://doi.org/10.1038/nmeth.2808

Semenova, I., Burakov, A., Berardone, N., Zaliapin, I., Slepchenko, B., Svitkina, T., … Rodionov, V. (2008). Actin Dynamics Is Essential for Myosin-Based Transport of Membrane Organelles. *Current Biology*, *18*(20), 1581–1586. http://doi.org/10.1016/j.cub.2008.08.070

Sommer, C., Straehle, C., Kothe, U., & Hamprecht, F. a. (2011). Ilastik: Interactive learning and segmentation toolkit. *2011 IEEE International Symposium on Biomedical Imaging: From Nano to Macro*, (1), 230–233. http://doi.org/10.1109/ISBI.2011.5872394

Zajac, A. L. L., Goldman, Y. E. E. E., Holzbaur, E. L. F. L. F., & Ostap, E. M. (2013). Local Cytoskeletal and Organelle Interactions Impact Molecular-Motor-Driven Early Endosomal Trafficking. *Current Biology*, *23*(13), 1173–80. http://doi.org/10.1016/j.cub.2013.05.015